

# Towards Interpretable Foundation Models for Retinal Fundus Images

Samuel Ofosu Mensah<sup>1,2\*</sup>, Camila Roa<sup>1\*</sup>, Kerol Djoumessi<sup>1</sup>, and Philipp Berens<sup>1,2</sup>

<sup>1</sup> Hertie Institute for AI in Brain Health, University of Tübingen, Germany

<sup>2</sup> Tübingen AI Center, University of Tübingen, Germany

{samuel.ofosu-mensah, maria-camila.roa-carvajal, philipp.berens  
}@uni-tuebingen.de

**Abstract.** Foundation models are used to extract transferable representations from large amounts of unlabeled data, typically via self-supervised learning (SSL). However, many of these models rely on architectures that offer limited interpretability, which is a critical issue in high-stakes domains such as medical imaging. We propose Dual-IFM, a foundation model that is interpretable-by-design in two ways: First, it provides local interpretability for individual images through class evidence maps that are faithful to the decision-making process. Second, it provides global interpretability for entire datasets through a 2D projection layer that allows for direct visualization of the model’s representation space. We trained our model on over 800,000 color fundus photography from various sources to learn generalizable, interpretable representations for different downstream tasks. Our results show that our model reaches a performance range similar to that of state-of-the-art foundation models with up to 16× the number of parameters, while providing interpretable predictions on out-of-distribution data. Our results suggest that large-scale SSL pretraining paired with inherent interpretability can lead to robust representations for retinal imaging.

**Keywords:** Foundation Model · Interpretable Model · Self-Supervised Learning · Color Fundus Photography.

## 1 Introduction

Foundation models are large-scale deep learning models trained on massive, diverse unlabeled datasets, typically via self-supervised learning (SSL), to learn general-purpose representations that can be adapted to downstream tasks [7]. In ophthalmology for example, RETFound [33] is the most widely used foundation model and inspired numerous studies applying such models to a range of ophthalmic imaging tasks [15,28,29]. While these models typically perform very well, they are not inherently interpretable, meaning the model cannot directly provide an explanation for each prediction [19,21]. Thus, several studies

---

\* These authors contributed equally.

on foundation models use post-hoc interpretable methods to explain the model’s decisions [29,28,33]. However, these explanations are often not faithful, since they do not align with the model’s decision-making process [2,27]. This lack of inherent interpretability limits the application of foundation models, especially in high-stakes domains such as medical imaging.

Understanding the model’s decision-making process is important, but so is understanding the semantic structure of the representations the model learns from the data [5]. Foundation models yield high-dimensional representations of input data, embedding semantic relationships in the geometric properties of the latent space. Although most interpretability methods aim to provide local explanations for individual predictions, they do not reveal whether the underlying representation space accurately captures semantic relationships, that is, whether semantically similar concepts such as disease grades are proximally embedded and whether the geometric structure reflects meaningful patterns rather than data artifacts or spurious correlations [1]. Visualizing representation spaces provides a complementary perspective to interpretability by exposing the global structure of what the model has learned [4,29,16]. As in these studies, embedding spaces are often visualized with neighbor embedding methods such as  $t$ -SNE [22]. However,  $t$ -SNE is non-parametric, which means it does not learn an explicit mapping from a high-dimensional input space to a low-dimensional output space and must be re-fitted every time new samples are added to a visualization, requiring a separate optimization step after model training, and for each, potentially very large dataset.

Motivated by these considerations, we introduce Dual-IFM, a two-way interpretable foundation model for color fundus photography (CFP) that combines local explanations with a visualization of global semantic representations, with ophthalmology as a high-stakes application domain. We trained our model using the BagNet architecture with the  $t$ -SimCNE algorithm [6]. The inherent local interpretability is provided by BagNet [8], which generates local class evidence maps, that are spatially averaged to form the model’s prediction, directly indicating which regions of the image contributed to a specific class prediction. The global interpretability comes from the 2D projection layer trained by  $t$ -SimCNE, which enables direct visualization of input images in the model’s representation space. By creating a parametric mapping, from the images to the 2D space, the model is able to embed new images into this space while avoiding additional fitting of other non-parametric visualization methods. Together, these components constitute a faithful framework for local and global interpretability, strengthening trust and usability of foundation models in high-stakes applications.

## 2 Methods

We trained the inherently-interpretable foundation model Dual-IFM on a large dataset of CFP. The model has a BagNet architecture as the backbone [8] and is trained to learn generalizable representations using the self-supervised contrastive  $t$ -SimCNE algorithm [6]. Together, this enables local interpretability by

providing class activation maps for individual CFPs and global interpretability by directly providing 2D visualizations of the embedding space.

## 2.1 Pretraining

Let  $\mathcal{X}$  denote the image space, where each image  $\mathbf{x} \in \mathcal{X} \subset \mathbb{R}^{H \times W \times C}$  with height  $H$ , width  $W$ , and  $C$  channels. We define  $\mathcal{T}$  as data augmentations. For each image  $\mathbf{x}$ , we sample two augmentation operators  $t, t' \sim \mathcal{T}$  and generate two views  $\tilde{\mathbf{x}} = t(\mathbf{x})$  and  $\tilde{\mathbf{x}}' = t'(\mathbf{x})$ . A mini-batch with size  $B$  images therefore yields  $2B$  augmented samples, which are used as positive and negatives pairs for contrastive learning, which aims to maximize the agreement between positive pairs relative to negatives in the batch [10]. Our goal is to learn a parametric representation function  $f_\theta : \mathcal{X} \rightarrow \mathcal{Z}$ , where  $\mathcal{Z} \subset \mathbb{R}^2$  is a 2-dimensional space that can be visualized. We decompose  $f_\theta$  into an encoder  $h_\psi : \mathcal{X} \rightarrow \mathcal{H} \subset \mathbb{R}^D$ , with  $D$  denoting the encoder feature dimension, and a projection head  $g_\phi : \mathcal{H} \rightarrow \mathcal{Z} \subset \mathbb{R}^2$ . The encoder produces a spatial feature map which is aggregated by global average pooling to obtain a  $D$ -dimensional feature vector  $\mathbf{h}$ , and the projection head maps  $\mathbf{h}$  to a 2D embedding  $\mathbf{z}$  (Fig. 1A). This yields a parametric mapping  $\mathbf{z} = g_\phi \circ h_\psi(\mathbf{x})$  that can be applied consistently to images after training to visualize the embedding space. By optimizing this objective the encoder learns meaningful representations from the retinal images useful for downstream tasks.

We trained our model in three stages using the  $t$ -SimCNE algorithm [6], which has the same contrastive objective as SimCLR [10]. However, it replaces the  $128D$  projection, on which the contrastive loss is computed, by a  $2D$  projection. This allows visualization of input images in the encoder’s representation space. Additionally,  $t$ -SimCNE replaces the cosine similarity, used by SimCLR’s NT-Xent loss with Euclidean similarity to improve visualization quality.

In stage one, we trained the full model, computing the loss at the  $128D$  output of the projector, similar to SimCLR. In stage two, the last layer of the projector is replaced with a two-dimensional output, which the authors refer to as dimensionality annealing. This layer is then aligned with the encoder’s representations, while the other layers remain frozen. Finally, in stage three, the full model is unfrozen and trained end-to-end with a lower learning rate.

The authors of  $t$ -SimCNE found that using Euclidean similarity for the full training yields the best visualizations. However, using cosine similarity during stage one improved the linear probe performance of the encoder’s representations, while slightly degrading the visualization. So unlike  $t$ -SimCNE, we used the NT-Xent loss for stage one, since our main objective was to obtain the best possible representations from the encoder for downstream tasks. For stages two and three we use the loss as proposed by  $t$ -SimCNE.

## 2.2 Fine-tuning

After pretraining, we introduce a classification head after the encoder, in addition to the already existing projection head to map high dimensional inputs to a 2D space (Fig. 1B). Following [14], we attached a  $1 \times 1$  convolution to the final feature

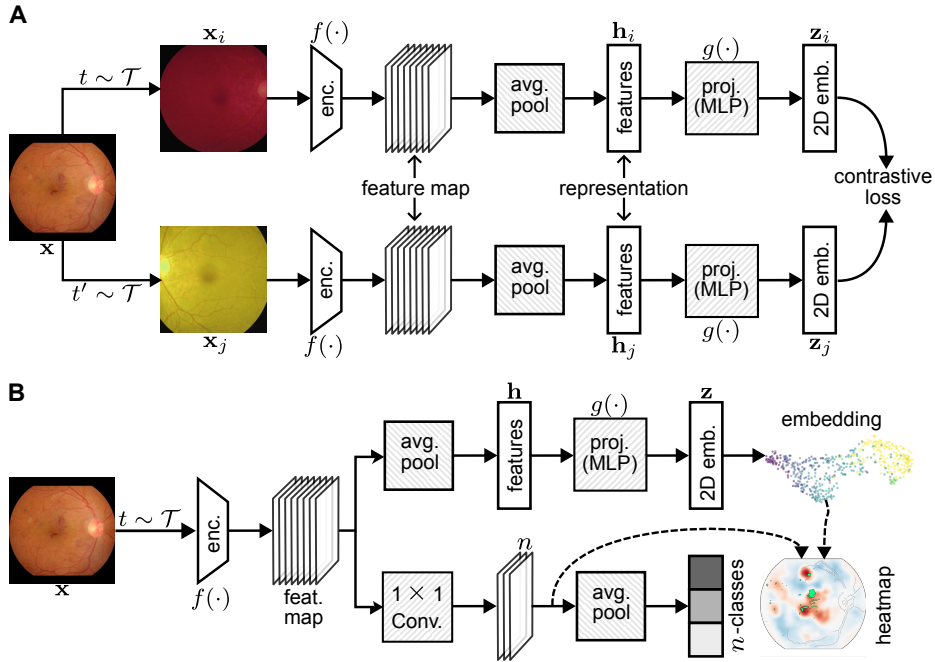


**Fig. 1. Overview of our inherently-interpretable foundation model.** (A) The encoder is pretrained from a large dataset of CFP with the  $t$ -SimCNE algorithm, to learn generalizable representations and a projection that maps input images to a 2D the visualization of the encoder’s representation space. (B) The model can be fine-tuned on downstream tasks while still allowing the visualization of the representation space.

map to produce  $n$  channel-wise activation maps (one per class). Then, we used global average pooling over each activation map yielding a corresponding class score and making the prediction an explicit spatial aggregation of local evidence. This new head can be used to train a linear-probe or to perform fine-tuning on downstream tasks.

### 2.3 Dual Interpretability

*Global interpretability:* The learned parametric mapping  $\mathbf{z} \in \mathbb{R}^2$  enables the direct embedding of unseen images into visualizations of the representation space (Fig. 1B). *Local interpretability:* The convolutional classifier provides explicit class evidence maps that directly highlight the regions of the image that contributed to the model’s predictions [14] (Fig. 1B).

### 2.4 Experimental details

To pretrain the model, we used the LARS optimizer [32] (batch size 1024, weight decay  $10^{-6}$ , base learning rate  $0.075 \times 32$ , which was reduced by a factor of 1000

in the last stage of training). We trained for 1000, 25 and 200 epochs for each stage. For stages one and three we used a cosine annealing schedule down to 0 with a warm-up of 10 epochs, while maintaining a constant learning rate for stage two. We pretrained the model with 8 NVIDIA H100 GPUs for 5 days and 11 hours. The full setup is available in our GitHub repository<sup>3</sup>.

Linear probing was performed by fitting a logistic regression classifier with elastic net penalty and class-balanced weights on the model’s representations for each dataset, and evaluating performance on a held-out test set. For fine-tuning, we trained the linear classification head with an AdamW [25] optimizer (weight decay  $10^{-4}$ , learning rate  $10^{-5}$  /  $10^{-4}$  for the encoder / classification head) for 5 epochs before unfreezing the full model. We continued training for a maximum of 50 epochs with early stopping. We used class-weighted cross entropy and five-fold cross-validation and report average performance across folds. For all datasets, we ensured that splits are performed at participant-level with stratification. We conducted the fine-tuning on one NVIDIA V100 GPU.

### 3 Results

We pretrained Dual-IFM on three CFP datasets that were preprocessed and filtered for quality [17]: EyePACS (567,384 images from 44,063 participants) [11], AREDS (110,690 images from 4,432 participants) [30], and UKBiobank (132,010 images from 72,711 participants) [31]. This yielded 802,360 images for pretraining. On held-out test sets, the model performed well on the in-distribution tasks of Diabetic Retinopathy (DR) detection and Age-related Macular Degeneration (AMD) classification (AUROC:  $0.822 \pm 0.054$  and  $0.928 \pm 0.004$ ) for fine-tuning, comparable to the retinal foundation model RETFound (AUROC:  $0.767 \pm 0.043$  and  $0.912 \pm 0.008$ ).

We then evaluated the quality of the representations learned by Dual-IFM across multiple disease-related tasks on out-of-distribution datasets: APTOS [18]

<sup>3</sup> [https://github.com/berenslab/interpretable\\_FM/](https://github.com/berenslab/interpretable_FM/)

**Table 1.** Linear-probe performance across various CFP tasks with model properties.

	ImageNet	SimCLR	Dual-IFM	RETFound
Local interpretability	+	+	+	-
Global interpretability	-	-	+	-
In-Domain training	-	+	+	+
APTOS	0.933	0.929	0.926	0.917
DeepDRiD	0.853	0.857	0.856	0.887
IDRiD	0.703	0.761	0.718	0.668
Messidor	0.802	0.867	0.868	0.797
Glaucoma	0.909	0.920	0.897	0.913
PAPILA	0.655	0.741	0.729	0.577
FIVES	0.882	0.918	0.928	0.837

(3,662 images), IDRiD [26] (516 images), DeepDRiD [24] (2,000 images) and Messidor-2 [12] (1,718 images) for DR grading, Glaucoma fundus [3] (1,544) and PAPILA [23] (488) for glaucoma grading and FIVES [20] for multi-disease classification. For all cases, we compared Dual-IFM with (1) a BagNet-33 initialized with ImageNet weights, (2) a BagNet-33 trained with standard SimCLR on our pretraining dataset and (3) the foundation model RETFound (Table 1).

### 3.1 Performance on eye disease classification

We found that Dual-IFM achieved as good or higher performance than a task-trained BagNet-33, indicating that the self-supervised domain specific pretraining can improve performance on downstream tasks (Tables 1 and 2). Additionally, we found that our model performed similarly to a SimCLR model and RETFound, indicating that adding the dual interpretability does not impair performance. The linear probing performance (Table 1) of Dual-IFM indicated that the learned representations were improved for 5/7 datasets compared to the task-trained baseline and to RETFound. While fine-tuning improved the performance for most datasets and models (Table 2) compared to linear probing, in the case of PAPILA and FIVES performance was lower, suggesting overfitting, possibly because we used the same fine-tuning settings for all datasets. Further performance gains, could be achieved by a hyperparameter search done for every dataset. Despite this limitation, Dual-IFM’s performance is on par with RETFound, in some cases surpassing it, suggesting that Dual-IFM learns generalizable features that support downstream retinal tasks.

### 3.2 Global interpretability through latent space visualization

Using the learned 2D projection, Dual-IFM enables global interpretability by embedding entire datasets into a directly visualizable representation space (Fig. 2). For the APTOS dataset, samples arranged along a curved manifold following DR severity: images of lower grades clustered in one region, while progressively higher grades occupied increasingly distinct regions (Fig. 2A, yellow to blue). The embedding for Glaucoma Fundus exhibited a similar structure, where samples arranged along a direction consistent with severity (Fig. 2B). For both datasets,

**Table 2.** Fine-tuning performance across 5-folds on various CFP tasks.

	ImageNet	SimCLR	Dual-IFM	RETFound
APTOS	0.937 ± 0.008	0.948 ± 0.004	0.945 ± 0.004	0.940 ± 0.004
DeepDRiD	0.896 ± 0.003	0.896 ± 0.005	0.897 ± 0.004	0.903 ± 0.007
IDRiD	0.790 ± 0.025	0.807 ± 0.024	0.799 ± 0.022	0.764 ± 0.032
Messidor	0.858 ± 0.009	0.864 ± 0.005	0.862 ± 0.006	0.845 ± 0.008
Glaucoma	0.910 ± 0.019	0.909 ± 0.007	0.924 ± 0.007	0.947 ± 0.007
PAPILA	0.616 ± 0.051	0.646 ± 0.028	0.648 ± 0.019	0.689 ± 0.058
FIVES	0.875 ± 0.019	0.886 ± 0.024	0.881 ± 0.016	0.936 ± 0.012

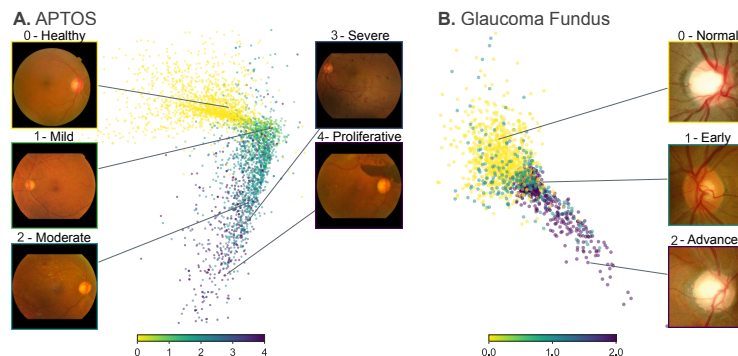


**Fig. 2. Global interpretability via representation space visualization.** 2D embeddings produced by the learned projection head for (A) APTOS ( $k$ -NN AUROC: 0.87) and (B) Glaucoma Fundus ( $k$ -NN AUROC: 0.85). The representation space of both dataset reveal a continuous transition of classes that mimic disease progression and potential borderline samples.

we observed overlap among disease grades highlighting potential borderline samples. Across all datasets, the representation space showed good disease severity clustering with average  $k$ -NN AUROC of 0.76 for the 2D map computed by our model, compared to 0.89/0.83 and 0.88/0.80 for a  $t$ -SNE / PCA post-hoc dimensionality reduction applied to the representation in the ImageNet and SimCLR models respectively. Further improvement of the 2D visualization is possible by aligning the projector to the representations of the model after fine-tuning, however we used the projector directly from pretraining. This alignment is computationally inexpensive, since only the projector is trained. It can be conducted once after, or potentially during, finetuning; however it is not always necessary to explore the embedding space.

### 3.3 Local interpretability through class evidence maps

We further studied the class evidence maps in Dual-IFM provided for individual CFPs through the BagNet architecture (Fig. 3). We found that incorporating a sparsity constraint in the fine-tuning process, as proposed by [14] did not impact classification performance (Fig. 3A). We selected the highest sparsity value before classification performance deteriorated. We measured the precision of the  $k = 10$  most activated patches to capture DR-related lesions on the IDRiD dataset, using Dual-IFM fine-tuned for binary DR classification (healthy vs diseased), following [13]. We obtained a high value of 0.674, indicating that the sparsity constraint improved the evidence maps by making them more localized. Qualitatively, the class evidence maps showed high activations for CFP regions with disease-related lesions (Fig. 3C-F), with much more overlap than the LRP [9] heatmaps from RETFound with a 0.384 precision (Fig. 3G,H). This shows the potential of Dual-IFM to provide clinically meaningful local interpretability.

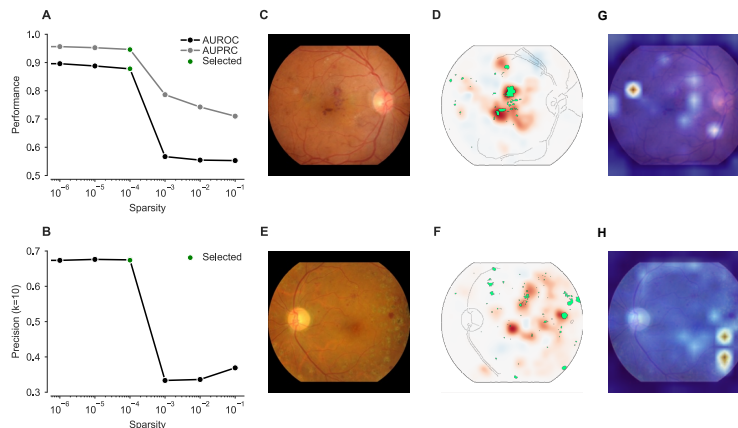


**Fig. 3. Local interpretability through class evidence maps.** (A) Fine-tuning performance for different values of sparsity. (B) Precision score for different values of sparsity. (C, E) Example fundus images. (D, F) Class evidence maps of Dual-IFM for these images with lesion annotations overlaid (green). (G, H) Shows LRP heatmaps for RETFound.

## 4 Discussion

We presented a dual interpretable foundation model for CFPs, that offers both local- and global-level interpretability. It achieved competitive performance across CFP benchmarks, demonstrating high-quality representations (linear probing) and adaptability to downstream tasks (fine-tuning). In some tasks, Dual-IFM with 18.3M parameters surpassed RETFound, even though RETFound is a substantially larger model with over 303M parameters, resulting in nearly twice the inference time (RETFound: 322 ms vs. Dual-IFM: 157 ms). Crucially, the Dual-IFM’s BagNet-based architecture provided inherent interpretability through class evidence maps that highlight lesion-relevant regions.

These properties make Dual-IFM well-suited for clinical deployment, where both accuracy and transparency are required. Additionally, training a BagNet is computationally expensive due to its small receptive field and the resulting large spatial feature maps; therefore, having pretrained weights that improve performance on downstream tasks, such as Dual-IFM, is advantageous.

Our work was limited to the use of CFP, as well as the absence of a systemic hyperparameter search during fine-tuning. Future work could extend to additional modalities (e.g. OCT and metadata) and different CNN-backbones to explore both local and global interpretability, in addition to other SSL objectives that could improve performance from pretraining. The inherent interpretability would also make it uniquely suited for a multimodal setting. In summary, our results suggest that both local and global interpretability can be obtained simultaneously with high quality representations in foundation models for medical images.

**Acknowledgments.** This project was supported by the Hertie Foundation and by the Deutsche Forschungsgemeinschaft under Germany’s Excellence Strategy with the Excellence Cluster 2064 “Machine Learning – New Perspectives for Science”, project number 390727645. PB is a member of the Else Kröner Medical Scientist Kolleg “ClinbrAIIn: Artificial Intelligence for Clinical Brain Research”. The authors thank the AREDS participants, and the AREDS Research Group for their valuable contribution to this research. Funding support for AREDS was provided by the National Eye Institute (N01-EY-0-2127). This research has been conducted using the UK Biobank Resource under Application Number (121699).

**Disclosure of Interests.** The authors declare no competing interests.

## References

1. Achtibat, R., Dreyer, M., Eisenbraun, I., Bosse, S., Wiegand, T., Samek, W., Lapuschkin, S.: From attribution maps to human-understandable explanations through concept relevance propagation. *Nature Machine Intelligence* **5**(9), 1006–1019 (2023)
2. Adebayo, J., Gilmer, J., Muelly, M., Goodfellow, I., Hardt, M., Kim, B.: Sanity checks for saliency maps. *Advances in neural information processing systems* **31** (2018)
3. Ahn, J.M., Kim, S., Ahn, K.S., Cho, S.H., Lee, K.B., Kim, U.S.: A deep learning model for the detection of both advanced and early glaucoma using fundus photography. *PLoS one* **13**(11), e0207982 (2018)
4. Ayhan, M.S., Neubauer, J., Uzel, M.M., Gelisken, F., Berens, P.: Interpretable detection of Epiretinal Membrane from optical coherence tomography with deep neural networks. *Scientific Reports* **14**(1), 8484 (2024)
5. Bengio, Y., Courville, A., Vincent, P.: Representation learning: A review and new perspectives. *IEEE transactions on pattern analysis and machine intelligence* **35**(8), 1798–1828 (2013)
6. Böhm, J.N., Berens, P., Kobak, D.: Unsupervised visualization of image datasets using contrastive learning. In: *International Conference on Learning Representations* (2023)
7. Bommasani, R., et al.: On the opportunities and risks of foundation models (2022)
8. Brendel, W., Bethge, M.: Approximating CNNs with bag-of-local-features models works surprisingly well on ImageNet. *International Conference on Learning Representations* (2019)
9. Chefer, H., Gur, S., Wolf, L.: Transformer interpretability beyond attention visualization. In: *Proceedings of the IEEE/CVF Conference on Computer Vision and Pattern Recognition (CVPR)*. pp. 782–791 (June 2021)
10. Chen, T., Kornblith, S., Norouzi, M., Hinton, G.: A simple framework for contrastive learning of visual representations. In: *International Conference on Machine Learning*. pp. 1597–1607. PMLR (2020)
11. Cuadros, J., Bresnick, G.: EyePACS: an adaptable telemedicine system for diabetic retinopathy screening. *Journal of diabetes science and technology* **3**(3), 509–516 (2009)
12. Decencière, E., Zhang, X., Cazuguel, G., Lay, B., Cochener, B., Trone, C., Gain, P., Ordóñez-Varela, J.R., Massin, P., Erginay, A., et al.: Feedback on a publicly distributed image database: the Messidor database. *Image Analysis & Stereology* pp. 231–234 (2014)

13. Djoumessi, K., Huang, Z., Kühlewein, L., Rickmann, A., Simon, N., Koch, L.M., Berens, P.: An inherently interpretable AI model improves screening speed and accuracy for early diabetic retinopathy. *PLOS Digital Health* **4**(5), e0000831 (2025)
14. Donteu, K.R.D., Ilanchezian, I., Kühlewein, L., Faber, H., Baumgartner, C.F., Bah, B., Berens, P., Koch, L.M.: Sparse activations for interpretable disease grading. In: *Medical Imaging with Deep Learning* (2023)
15. Du, J., Guo, J., Zhang, W., Yang, S., Liu, H., Li, H., Wang, N.: Ret-clip: A retinal image foundation model pre-trained with clinical diagnostic reports. In: *International conference on medical image computing and computer-assisted intervention*. pp. 709–719. Springer (2024)
16. Engelmann, J., Bernabeu, M.O.: Training a high-performance retinal foundation model with half-the-data and 400 times less compute. *Nature Communications* **16**(1), 6862 (Jul 2025)
17. Gervelmeyer, J., Müller, S., Huang, Z., Berens, P.: Fundus image toolbox: A python package for fundus image processing. *Journal of Open Source Software* **10**(108), 7101 (Apr 2025)
18. Goha, E.F., Chen, Z., Lima, W.X.: APTOS 2019 blindness detection competition dataset (Dec 2024)
19. Grote, T.: The allure of simplicity: On interpretable machine learning models in healthcare. *Philosophy of Medicine* **4**(1) (2023)
20. Jin, K., Huang, X., Zhou, J., Li, Y., Yan, Y., Sun, Y., Zhang, Q., Wang, Y., Ye, J.: FIVES: A fundus image dataset for artificial intelligence based vessel segmentation. *Scientific data* **9**(1), 475 (2022)
21. Kazmierczak, R., Berthier, E., Frehse, G., Franchi, G.: Explainability and vision foundation models: A survey. *Information Fusion* **122**, 103184 (2025)
22. Kobak, D., Berens, P.: The art of using t-SNE for single-cell transcriptomics. *Nature communications* **10**(1), 5416 (2019)
23. Kovalyk, O., Morales-Sánchez, J., Verdú-Monedero, R., Sellés-Navarro, I., Palazón-Cabanes, A., Sancho-Gómez, J.L.: PAPILA: Dataset with fundus images and clinical data of both eyes of the same patient for glaucoma assessment. *Scientific Data* **9**(1), 291 (2022)
24. Liu, R., Wang, X., Wu, Q., Dai, L., Fang, X., Yan, T., Son, J., Tang, S., Li, J., Gao, Z., et al.: Deepdrid: Diabetic retinopathy—grading and image quality estimation challenge. *Patterns* **3**(6) (2022)
25. Loshchilov, I., Hutter, F.: Decoupled weight decay regularization. In: *International Conference on Learning Representations* (2019)
26. Porwal, P., Pachade, S., Kamble, R., Kokare, M., Deshmukh, G., Sahasrabudhe, V., Meriaudeau, F.: Indian diabetic retinopathy image dataset (IDRiD): a database for diabetic retinopathy screening research. *Data* **3**(3), 25 (2018)
27. Rudin, C.: Stop explaining black box machine learning models for high stakes decisions and use interpretable models instead. *Nature machine intelligence* **1**(5), 206–215 (2019)
28. Shi, D., Zhang, W., Yang, J., Huang, S., Chen, X., Xu, P., Jin, K., Lin, S., Wei, J., Yusufu, M., et al.: A multimodal visual–language foundation model for computational ophthalmology. *NPJ digital medicine* **8**(1), 381 (2025)
29. Sun, Y., Tan, W., Gu, Z., He, R., Chen, S., Pang, M., Yan, B.: A data-efficient strategy for building high-performing medical foundation models. *Nature Biomedical Engineering* pp. 1–13 (2025)
30. The Age-Related Eye Disease Study Research Group: The age-related eye disease study (AREDS): design implications AREDS report no. 1. *Controlled clinical trials* **20**(6), 573 (1999)

31. Warwick, A.N., Curran, K., Hamill, B., Stuart, K., Khawaja, A.P., Foster, P.J., Lotery, A.J., Quinn, M., Madhusudhan, S., Balaskas, K., et al.: UK Biobank retinal imaging grading: methodology, baseline characteristics and findings for common ocular diseases. *Eye* **37**(10), 2109–2116 (2023)
32. You, Y., Gitman, I., Ginsburg, B.: Large batch training of convolutional networks (2017)
33. Zhou, Y., Chia, M.A., Wagner, S.K., Ayhan, M.S., Williamson, D.J., Struyven, R.R., Liu, T., Xu, M., Lozano, M.G., Woodward-Court, P., et al.: A foundation model for generalizable disease detection from retinal images. *Nature* **622**(7981), 156–163 (2023)